Design, control and comparative analysis of an LCLC coupling hybrid active power filter

Zeng Xiang[1,2], Ying Pang[1,2], Lei Wang[3] ✉, Chi-Kong Wong[1], Chi-Seng Lam[1,4], Man-Chung Wong[1,2,4]

[1]*Department of Electrical and Computer Engineering, Faculty of Science and Technology, University of Macau, Macau, People's Republic of China*
[2]*State Key Laboratory of Internet of Things for Smart City, University of Macau, Macau, People's Republic of China*
[3]*College of Electrical and Information Engineering, Hunan University, Changsha, People's Republic of China*
[4]*State Key Laboratory of Analog and Mixed-Signal VLSI, University of Macau, Macau, People's Republic of China*
✉ *E-mail: jordanwanglei@gmail.com*

Abstract: This study provides the design, control and comparative analysis of the proposed LCLC coupling hybrid active power filter (LCLC-HAPF). Compared with the conventional L filter coupling active power filters (APFs), LC filter and LCL filter coupling HAPFs (LC-HAPFs and LCL-HAPFs), the proposed LCLC-HAPF provides better switching frequency harmonics elimination, lower dc-link voltage rating and switching loss. Although the LCLC-HAPF has some advantages, two main challenges will still be confronted in practical implementations. Those are stability problems caused by resonance of LCLC filter, and parameter design for the LCLC filter. In this study, a new active damping method is proposed to overcome the high order resonance problem existing in the proposed LCLC-HAPF. After that, the stability analysis and parameter design are given for the proposed LCLC-HAPF. Finally, the effectiveness of the proposed LCLC-HAPF topology is validated through both simulation and experimental studies in comparison with the conventional APFs and HAPFs.

1 Introduction

Low power factor and current harmonic distortion are considered as two major power quality issues in three-phase three-wired power system. To solve the power quality issues, different power quality compensators have been proposed among the existing literature [1–33].

Before the advent of power electronics, passive power filters (PPFs) [1] and static var compensators (SVCs) [2, 3] have been widely used to compensate reactive power and/or suppress current harmonics due to the desirable characteristics of the low cost and simplicity. However, both PPFs and SVCs have the disadvantages of slow response, poor dynamic performance and resonance problems. To address the above potential problems in PPFs and SVCs, the L filter coupling active power filters (APFs) were proposed. However, the APFs require high-power rating voltage source inverters (VSIs) [4], which lead to the increase of the initial cost and power loss. Some hybrid APFs (HAPFs) topologies have been proposed to overcome the limitations of the traditional APFs. There are two common topologies. One is the active filter added in parallel to a fundamental resonance circuit forming the injection-type HAPFs (IT-HAPFs) [5–9], and the other is the active filter added in series to the passive filters (series HAPFs) [10–18]. In the first case, the topology only outputs harmonic currents, therefore, the power rating of the active part is low. The series resonance circuit must tune at the fundamental frequency [5]. However, the ageing of the components will cause the resonance point to shift, which will eventually affect the performance. On the other hand, additional compensators are required to accomplish more functionalities. For example, thyristor-controlled reactors are increased to compensate reactive and unbalanced current [7, 9]. For the second case, the most common types are LC-coupling HAPFs (LC-HAPFs), the required dc-link voltage rating of the VSIs is also small since most of the voltage drop occurs on the capacitor. Meanwhile, it can compensate harmonics and reactive currents without additional compensators. In addition, SVC coupling HAPFs (SVC-HAPFs) are studied in [15–18], which have the characteristics of a wider compensation range than LC-HAPFs.

However, the topology is more complicated than that of LC-HAPFs.

For the two type HAPFs discussed above, there is little discussion about high-frequency harmonic suppression. For most series HAPFs, the passive part is the LC filter. However, the LC filter cannot suppress the high order harmonic current well, unless a big inductance value is used. Otherwise, the switching frequency sideband harmonics are difficult to meet the IEEE standard requirements [19]. To reduce the high order harmonic current, the LCL filter coupling HAPFs (LCL-HAPFs) have been reported in [20–26]. Compared with the L filter and LC filter with −20 dB/dec attenuation, the LCL filter can obtain a −60 dB/dec attenuation as described in [21]. In addition, if the resonance frequency, is set to bigger than 2 times the highest compensated frequency that will not affect the compensation performance of the LCL-HAPFs [22]. However, the LCL-HAPFs use a similar dc-link voltage as that of APFs. To combine the advantages of LC filter and LCL filter, hybrid distribution static synchronous compensators (hybrid-DSTATCOMs) topology is proposed in [27]. And, a passive damping (PD) resistor is inserted into the hybrid-DSTATCOMs to overcome the system instability. However, the PD resistors can cause extra power loss and thereby reduce the system efficiency. Moreover, the additional resistors can weaken the high order frequency harmonic attenuation.

Actually, the active damping (AD) methods have been developed for LCL-HAPFs applications [28–33]. Among them, the virtual resistor (VR) methods are the most popular ones [28–32]. Either the capacitor current [28–30] or the capacitor voltage is feeding back [31–32] to the system in order to obtain satisfactory performances without causing the system instability. However, these VR methods require additional high-precision sensors to get extra feedback information, which can increase the cost. To avoid additional sensors, another AD method is proposed in [33], which is directly used in the grid-side current as a feedback signal.

In this paper, an LCLC coupling HAPF (LCLC-HAPF) is proposed for reactive power and current harmonics compensation. Compared with the existing APFs and HAPFs, the LCLC-HAPF provides better high-frequency harmonics suppression capability, lower VSIs power rating, lower switching loss and smaller inductor

Table 1 Characteristics of different compensators

	Response time	Resonance problem	DC-link voltage	High order harmonics attenuation	Power loss	Cost
PPFs [1]	**slow**	**yes**	—	—	small	low
SVCs [2, 3]	**slow**	**yes**	—	—	medium	low
APFs [4, 5]	fast	no	**high**	**large**	**large**	**high**
LC-HAPFs [11–19]	medium	no	low	**large**	medium	medium
LCL-HAPFs [24–30]	fast	no	**high**	small	**large**	**high**
hybrid-DSTATCOMs [27]	medium	no	low	medium	medium	medium
proposed LCLC-HAPF	medium	no	low	small	small	medium

Note: Bold text means undesirable characteristics.
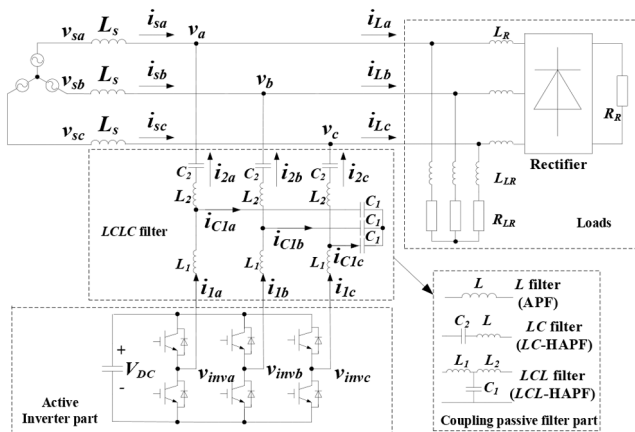
Fig. 1 *Circuit configurations of the proposed LCLC-HAPF*

Fig. 2 *Equivalent single-phase circuits*
(a) APF,
(b) LC-HAPF,
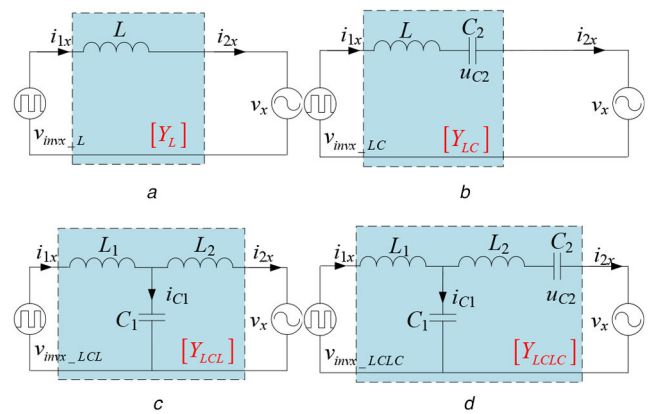*(c)* LCL-HAPF,
(d) LCLC-HAPF

value requirement. Based on the above discussions, the characteristics of different compensators are summarised in Table 1.

In addition, in order to guarantee the stability of the LCLC-HAPF system, the AD methods can be used to mitigate the resonance problem. However, no AD methods for LCLC filters have been reported before. And the AD method in [33] is not directly applicable to LCLC-HAPF. In this paper, an AD method is proposed for the LCLC-HAPF to further reduce the switching frequency sideband harmonic current and to avoid the high order resonance phenomenon existed in the LCLC-HAPF.

The main contributions of this paper can be summarised as follows:

- An LCLC-HAPF is proposed, with the distinctive characteristics of a lower dc-link voltage rating, lower switching loss and better harmonic elimination than conventional APFs and HAPFs.
- A new AD method is proposed for LCLC-HAPF to avoid potential stability issues.
- Comparative analysis of the dc-link voltage requirements and high-frequency harmonic attenuation capability are provided among the different topologies.
- Its parameter design method and control strategy are proposed based on considerations of the compensation function and high-frequency harmonic current elimination.

The rest of this paper is organised as follows. In Section 2, the circuit configurations are provided for the APF, the HAPFs (LC and LCL filters) and the proposed LCLC-HAPF, and their comparative study is provided. In Section 3, a control strategy based on the AD method is proposed for the LCLC-HAPF to avoid the resonance problem, and its stability issues are also discussed. In Section 4, the parameter design of the LCLC filter is introduced. Then representative simulation and experimental results are provided for the conventional APF, LC-HAPF, LCL-HAPF and the proposed LCLC-HAPF in Section 5, respectively. Finally, the conclusion is drawn in Section 6.

2 Comparative analysis of APF, LC-HAPF, LCL-HAPF and the proposed LCLC-HAPF

In this section, the comparative analysis of APF, LC-HAPF, LCL-HAPF and the proposed LCLC-HAPF are provided and discussed. Their circuit configurations are introduced in Section 2.1. Then, their corresponding comparisons in terms of dc-link voltage and switching frequency harmonic attenuation are provided in Sections 2.2 and 2.3, respectively.

2.1 Circuit configuration of APF, LC-HAPF, LCL-HAPF and the proposed LCLC-HAPF

Fig. 1 shows the circuit configurations of three-phase three-wired LCLC-HAPF. In this paper, the subscript 'x' denotes phases $x = a$, b, c, v_{sx}, v_x and v_{invx} are the source phase voltage, load voltage and inverter voltage, respectively. i_{sx}, i_{Lx}, i_{1x}, i_{2x} and i_{C1x} are source current, load current, inverter-side current, grid-side current, and current through C_1, respectively. The coupling capacitor C_2 in LCLC filter can provide a large voltage drop between v_x and v_{invx}. And, L_1, L_2 and C_1 are used to eliminate the harmonic current. If the passive part is replaced by the coupling L filter, LC filter and LCL filter, it becomes APF, LC-HAPF and LCL-HAPF, respectively.

Based on Fig. 1, the single-phase equivalent circuits of APF, LC-HAPF, LCL-HAPF and LCLC-HAPF are shown in Fig. 2. In Fig. 2, v_{invx_y} represents the inverter output voltage under different passive filtering circuits, where the subscript 'y' denotes different coupling impedances of L, LC, LCL and LCLC filters. In Fig. 2, matrix $[Y_y]$ is the coupling admittance of the two-port network. Under the same system and loading conditions, the load voltage v_x and the grid-side current i_{2x} are the same idea case, while the inverter voltage v_{invx_y} and the coupling admittance $[Y_y]$ are different. In the following, the total inductance of each filtering circuit topology in Fig. 2 is kept the same for a fair comparison, which is $L = L_1 + L_2$.

2.2 Comparisons of inverter voltage and dc-link voltage

According to the equivalent single-phase circuits in Fig. 2, the inverter-side current and grid-side current can be expressed as:

$$\begin{bmatrix} i_{1x\_y} \\ i_{2x} \end{bmatrix} = \begin{bmatrix} Y_{11\_y} & Y_{12\_y} \\ Y_{21\_y} & Y_{22\_y} \end{bmatrix} \cdot \begin{bmatrix} v_{\text{inv}x\_y} \\ v_x \end{bmatrix} \quad (1)$$

where Y_{11_y}, Y_{12_y}, Y_{21_y}, Y_{22_y} are the admittance parameters of two-port network [34]. In (1), the grid-side current i_{2x} and inverter voltage $v_{\text{inv}x\_y}$ can be expressed in terms of fundamental and harmonic components as follows:

$$i_{2x} = i_{2x1} + \sum_{n=2}^{\infty} i_{2xn} = v_{\text{inv}x\_y1} \cdot Y_{21\_y1} + v_x \cdot Y_{22\_y1}$$
$$+ \sum_{n=2}^{\infty} v_{\text{inv}x\_yn} \cdot Y_{21\_yn} \quad (2)$$

$$v_{\text{inv}x\_y} = v_{\text{inv}x\_y1} + \sum_{n=2}^{\infty} v_{\text{inv}x\_yn}$$
$$= \frac{i_{2x1} - v_x \cdot Y_{22\_y1}}{Y_{21\_y1}} + \sum_{n=2}^{\infty} \frac{i_{2xn}}{Y_{21\_yn}} \quad (3)$$

where the subscript '1' denotes the fundamental component, the subscript 'n' denotes the harmonic component. Equation (3) can be re-written in cosine form as:

$$v_{\text{inv}x\_y} = \frac{\sqrt{2} \cdot I_{2x1}\cos(\omega t + \varphi 1) - \sqrt{2} \cdot Y_{22\_y1} \cdot V_x\cos(\omega t)}{Y_{21\_y1}}$$
$$+ \sum_{n=2}^{\infty} \frac{\sqrt{2} \cdot I_{2xn}\cos(\omega_n t + \varphi_n)}{Y_{21\_yn}} \quad (4)$$

where V_x is the root-mean-square (rms) value of the source phase voltage, I_{2x1} and I_{2xn} are the rms of the grid-side fundamental current and the nth-order harmonic current, respectively. φ_1 is the phase angle between v_x and i_{2x1}, φ_n is the phase angle between v_x and i_{2xn}. The Y_{22_yn} and Y_{21_yn} for APF, LC-HAPF, LCL-HAPF, LCLC-HAPF can be expressed as follows:

$$Y_{22\_Ln} = Y_{21\_Ln} = \frac{1}{jn\omega L} \quad (5)$$

$$Y_{22\_LCn} = Y_{21\_LCn} = \frac{jn\omega C_2}{1 - (n\omega)^2 LC_2} \quad (6)$$

$$Y_{22\_LCLn} = \frac{1 - (n\omega)^2 L_1 C_1}{-j(n\omega)^3 L_1 L_2 C_1 + jn\omega(L_1 + L_2)} \quad (7)$$

$$Y_{21\_LCLn} = \frac{1}{-j(n\omega)^3 L_1 L_2 C_1 + jn\omega(L_1 + L_2)} \quad (8)$$

$$Y_{22\_LCLCn} = \frac{-j(n\omega)^3 L_1 C_1 C_2 + jn\omega C_2}{(n\omega)^4 L_1 L_2 C_1 C_2 s^4 - (n\omega)^2 (L_1 C_1 + LC_2) + 1} \quad (9)$$

$$Y_{21\_LCLCn} = \frac{jn\omega C_2}{(n\omega)^4 L_1 L_2 C_1 C_2 - (n\omega)^2 (L_1 C_1 + LC_2) + 1} \quad (10)$$

According to (4)–(10) with $n = 1$, the fundamental inverter voltage v_{inv_y1} for APF, LC-HAPF, LCL-HAPF, LCLC-HAPF can be expressed as follows:

$$v_{\text{inv}x\_L1} = \sqrt{2}V_x\cos(\omega_1 t) + \sqrt{2}\omega_1 L I_{2x1}\cos(\omega_1 t + \varphi_1) \quad (11)$$

$$v_{\text{inv}x\_LC1} = \left(\sqrt{2}V_x\cos(\omega_1 t) - \frac{\sqrt{2}I_{2x1}\cos(\omega_1 t + \varphi_1)}{\omega_1 C_2}\right)$$
$$+ \sqrt{2}\omega_1 L I_{2x1}\cos(\omega_1 t + \varphi_1) \quad (12)$$

$$v_{\text{inv}x\_LCL1} \simeq \sqrt{2}V_x\cos(\omega_1 t)(1 - \omega_1^2 L_1 C_1)$$
$$+ \sqrt{2}\omega_1 L I_{2x1}\cos(\omega_1 t + \varphi_1) \quad (13)$$

$$v_{\text{inv}x\_LCLC1} \simeq \left(\sqrt{2}V_x\cos(\omega_1 t) - \frac{\sqrt{2}I_{2x1}\cos(\omega_1 t + \varphi_1)}{\omega_1 C_2}\right)$$
$$(1 - \omega_1^2 L_1 C_1) + \sqrt{2}\omega_1 L I_{2x1}\cos(\omega_1 t + \varphi_1) \quad (14)$$

On the other hand, with (4)–(10) and $n > 1$, the inverter voltage at the harmonic frequency $v_{\text{inv}x\_yn}$ for APF, LC-HAPF, LCL-HAPF, LCLC-HAPF can be deduced as follows:

$$v_{\text{inv}x\_Ln} = \sqrt{2}\omega_n L I_{2xn}\cos(n\omega_1 t + \varphi_n) \quad (15)$$

$$v_{\text{inv}x\_LCn} = \sqrt{2}\left(\omega_n L - \frac{1}{\omega_n C_2}\right)I_{2xn}\cos(n\omega_1 t + \varphi_n) \quad (16)$$

$$v_{\text{inv}x\_LCLn} = \sqrt{2}(\omega_n L + \omega_n^3 L_1 L_2 C_1)I_{2xn}\cos(n\omega_1 t + \varphi_n) \quad (17)$$

$$v_{\text{inv}x\_LCLCn} =$$
$$\sqrt{2}\left(\omega_n L - \frac{1}{\omega_n C_2} + \omega_n^3 L_1 L_2 C_1 + \frac{\omega_n L_1 C_1}{C_2}\right)I_{2xn}\cos(n\omega_1 t + \varphi_n) \quad (18)$$

In general, the required dc-link voltage of the inverters should be larger than the peak value of the inverter output voltage ($v_{\text{inv}x\_y}$) to ensure proper compensation. According to (4), the $v_{\text{inv}x\_y}$ is composed of fundamental and harmonic components. Therefore, the peak value of $v_{\text{inv}x\_y}$ is related to the amplitude and phase of each component. It is very difficult to solve the peak value of $v_{\text{inv}x\_y}$. Considering the worst phase relation between each harmonic component, that is, $v_{\text{inv}x\_y}$ obtains the maximum value. Equation (4) can be expressed as:

$$v_{\text{inv}x\_y\text{max}} = \sqrt{3} \cdot \left(\left|\frac{\sqrt{2} \cdot V_x \cdot Y_{22\_y1} - \sqrt{2} \cdot I_{2x1}}{Y_{21\_y1}}\right| + \sum_{n=2}^{\infty} \left|\frac{\sqrt{2} \cdot I_{2xn}}{Y_{21\_yn}}\right|\right) \quad (19)$$

where $\sqrt{3}$ is the three-phase three-wire system coefficient. Assuming m is the pulse width modulation index, which is normally smaller than 1 ($m \leq 1$), according to (19), the minimum required dc-link voltage V_{dc_y} can be expressed as:

$$V_{\text{dc}\_y} = \frac{1}{m}v_{\text{inv}x\_y\text{max}} > \sqrt{6}\left(\underbrace{\left|\frac{Y_{22\_y1} \cdot V_x - I_{2x1}}{Y_{21\_y1}}\right|}_{v_{\text{inv}x\_y1}} + \underbrace{\sum_{n=2}^{\infty}\left|\frac{I_{2xn}}{Y_{21\_yn}}\right|}_{v_{\text{inv}x\_yn}}\right) \quad (20)$$

where the fundamental component ($v_{\text{inv}x\_y1}$) can be obtained by (11)–(14) and harmonic component ($v_{\text{inv}x\_yn}$) can be obtained by (15)–(18).

According to the above analysis, R_{dc_y} is defined as the required dc-link voltage ratio between LCLC-HAPF and other filters ($R_{\text{dc}\_y} = V_{\text{dc}\_LCLC}/V_{\text{dc}\_y}$, $y = L$, LC, LCL) as shown in Fig. 3. When the coupling filter is L filter as an APF, it has $R_{\text{dc}\_L} = V_{\text{dc}\_LCLC}/V_{\text{dc}\_L}$. When $R_{\text{dc}\_L} = 0.5$, it means that the required dc-link voltage of LCLC-HAPF is half of that of APF. As shown in Fig. 3, R_{dc_L} is less than 0.5 as a result, therefore, the LCLC-HAPF requires dc-link voltage is 50% less than that of APF. Similarly, we can obtain the following results:

(i) The LCLC-HAPF requires a dc-link voltage, which is 50% less than that of APF and LCL-HAPF.
(ii) Only in a small region, LC-HAPF obtains a dc-link voltage that can be comparable to the LCLC-HAPF one, but its harmonic
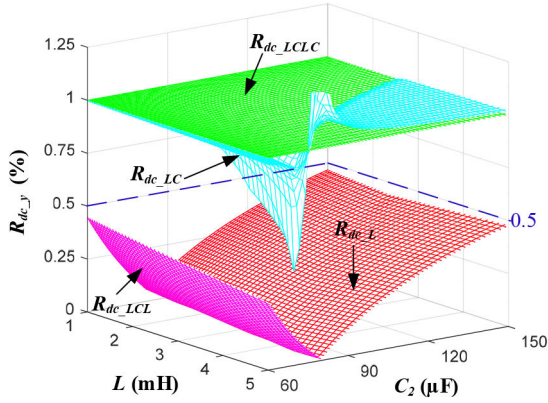
Fig. 3 R_{dc_y} between LCLC-HAPF and other filters with varying L and C_2

Fig. 4 Bode plots of Y_{21_LCLCn}/Y_{21_Ln}, Y_{21_LCLCn}/Y_{21_LCn} and Y_{21_LCLCn}/Y_{21_LCLn}

attention capability is not as good as LCLC-HAPF one (This characteristic will be explained in the following sections).

2.3 Comparisons of switching frequency harmonic attenuation

This section aims to prove that the LCLC part of the proposed LCLC-HAPF obtains attractive high-frequency harmonic attenuation, thus low cost and smaller volume of filtering inductor can be selected for the LCLC-HAPF. According to (5), (6), (9), (10), the comparative bode plots of the passive parts of the LC-HAPF, LCL-HAPF and LCLC-HAPF can be plotted in Fig. 4 where $C_1 = 10$ µF, $C_2 = 120$ µF, $L_1 = 1$ mH, $L_2 = 2.3$ mH, $L = 3.3$ mH. The bode diagram can be divided into three segments: segment I, segment II and segment III. The dividing line is the four resonance points ω_{reLC}, ω_{reLCL}, $\omega_{re1LCLC}$ and $\omega_{re2LCLC}$ (in radians per second) or f_{reLC}, f_{reLCL}, $f_{re1LCLC}$ and $f_{re2LCLC}$ (in hertz). According to (5), (6), (9), (10), the resonance points can be calculated as follows:

$$\omega_{reLC} = \frac{1}{\sqrt{LC_2}} \tag{21}$$

$$\omega_{reLCL} = \sqrt{\frac{L}{L_1 L_2 C_1}} \tag{22}$$

$$\omega_{re1LCLC} = \sqrt{\frac{L_1 C_1 + LC_2 - \sqrt{L_1^2 C_1^2 + L^2 C_2^2 + 2L_1^2 C_1 C_2 - 2L_1 L_2 C_1 C_2}}{2L_1 L_2 C_1 C_2}}$$
$$\simeq \sqrt{\frac{L}{LC_2}} = \omega_{reLC} \tag{23}$$

$$\omega_{re2LCLC} = \sqrt{\frac{L_1 C_1 + LC_2 + \sqrt{L_1^2 C_1^2 + L^2 C_2^2 + 2L_1^2 C_1 C_2 - 2L_1 L_2 C_1 C_2}}{2L_1 L_2 C_1 C_2}}$$
$$\simeq \sqrt{\frac{L}{L_1 L_2 C_1}} = \omega_{reLCL} \tag{24}$$

where ω_{reLC} and ω_{reLCL} are the resonance points of the LC filter of the LC-HAPF and LCL filter of the LCL-HAPF, respectively, and $\omega_{re1LCLC}$ and $\omega_{re2LCLC}$ are the two resonance points of the LCLC filter of the proposed LCLC-HAPF.

We focus on the comparison of high-frequency characteristics (in segment III). The slope of Y_{21_LCLCn}/Y_{21_LCLn} is 0 dB/dec, and the slope of Y_{21_LCLCn}/Y_{21_Ln}, Y_{21_LCLCn}/Y_{21_LCn} are −40 dB/dec in Fig. 4. The $20\lg(Y_{21\_yn})$ is the attenuation of corresponding different filters, the subscript 'y' denotes different filters, $y = $ L, LC, or LCL. $A_{tten\_y} = 20\lg(Y_{21\_LCLCn}/Y_{21\_yn}) = 20\lg(Y_{21\_LCLCn}) - 20\lg(Y_{21\_yn})$, which is defined as the attenuation difference between LCLC filter and other filters at switching frequency f_s. Therefore, if $A_{tten\_y} = 0$ dB, which means LCLC filter and y have
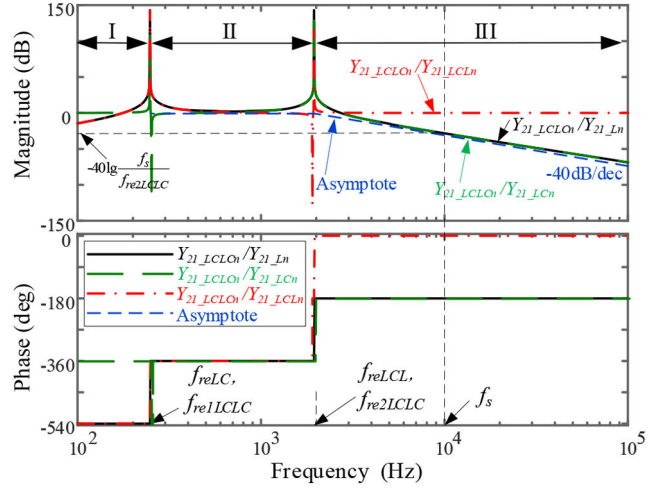
the same attenuation. if $A_{tten\_y} > 0$ dB, the attenuation of y is bigger than LCLC filter. Inversely, $A_{tten\_y} < 0$ dB, the attenuation of y is less than LCLC filter.

In Fig. 4, $A_{tten\_LCL} = 0$ dB, $A_{tten\_L} = A_{tten\_LC}$. The A_{tten_L} can be obtained by the asymptote of Y_{21_LCLCn}/Y_{21_Ln}. The asymptotic transition frequency is $f_{re2LCLC}$ where the magnitude equal to 0 dB. Thus, A_{tten_L} is equal to the slope of Y_{21_LCLCn}/Y_{21_Ln} multiplied by the logarithmic form of the distance between f_s and $f_{re2LCLC}$, which can be expressed as:

$$A_{tten\_L} = A_{tten\_LC} = -40\lg\frac{f_s}{f_{re2LCLC}} \tag{25}$$

where −40 dB/dec is the slope of Y_{21_LCLCn}/Y_{21_LCn}, $\lg(f_s/f_{re2LCLC})$ is logarithmic form of the distance between f_s and $f_{re2LCLC}$.

According to Fig. 4, the advantage of LCLC filter is that it has the same attractive attenuation as LCL filter, and a $40\lg(f_s/f_{re2LCLC})$ dB higher than that of L and LC filter. Thus, low cost and smaller volume of the inductor can be selected for the LCLC-HAPF under the same attenuation at f_s.

2.4 Summary

Based on the discussions of dc-link voltage requirement in Section 2.2 and high-frequency harmonic attenuation in Section 2.3. These two items will be reflected into switching frequency sideband harmonic current I_{h_s}. I_{h_s} is caused by the switching frequency sideband harmonic voltage V_{h_s} which is positively correlated with the dc-link voltage [35]. According to Ohm's law, the current (I_{h_s}) is directly proportional to the voltage (V_{h_s}) and inversely proportional to the impedance ($1/Y_{21\_yn}$). Therefore, I_{h_s} is directly proportional to V_{dc} and high-frequency attenuation (Y_{21_yn}). R_{Ih_sy} denotes I_{h_s} ratio between LCLC-HAPF and APF, LC-HAPF, LCL-HAPF. R_{Ih_sy} can be expressed as:

$$R_{Ih\_sy} = R_{dc\_y} \cdot \left.\frac{Y_{21\_LCLCn}}{Y_{21\_yn}}\right|_{n = f_s/f_1} \tag{26}$$

where Y_{21_LCLCn}/Y_{21_yn} is the high-frequency attenuation ratio between the passive part of the LCLC-HAPF and those of the APF, LC-HAPF and LCL-HAPF. For LCL filter, Y_{21_LCLCn}/Y_{21_LCLn} is equal to 0. According to (25), the Y_{21_LCLCn}/Y_{21_Ln} and Y_{21_LCLCn}/Y_{21_LCn} at f_s/f_1 can be obtained as follows:

$$\left.\frac{Y_{21\_LCLCn}}{Y_{21\_Ln}}\right|_{n = f_s/f_1} = \left.\frac{Y_{21\_LCLCn}}{Y_{21\_LCn}}\right|_{n = f_s/f_1} = \left(\frac{f_{re2LCLC}}{f_s}\right)^2 \tag{27}$$

Table 2 Comparison of the passive parts of the APF, LC-HAPF, LCL-HAPF and LCLC-HAPF in terms of dc-link voltage, high order harmonic attenuation and switching frequency sideband harmonic current

Compensator	R_{dc_y} in Fig. 3	A_{tten_y}, dB in Fig. 4	R_{Ih_sy} in (26) and (27)
APF	<0.5	$-40\lg(f_s/f_{res2LCLC})$	$0.5(f_{re2LCLC}/f_s)^2 < 1/8$
LC-HAPF	$\simeq 1$ (<1)	$-40\lg(f_s/f_{res2LCLC})$	$(f_{re2LCLC}/f_s)^2 < 1/4$
LCL-HAPF	<0.5	0	<1/2
LCLC-HAPF	1	0	1
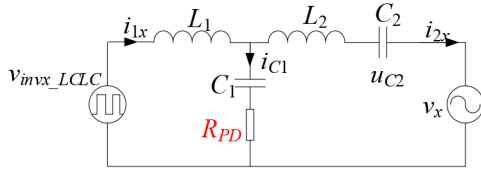
Fig. 5 *Conventional PD method for LCLC-HAPF*

In generally, $f_{res2LCLC}$ is required to be less than $0.5f_s$ [22], which means that both Y_{21_LCLCn}/Y_{21_Ln} and Y_{21_LCLCn}/Y_{21_LCn} are less than 1/4 at f_s/f_1 according to (27). In addition, Y_{21_LCLCn}/Y_{21_LCLn} is equal to 1 at f_s/f_1.

Based on the above discussions, the comparative characteristics of the passive part of the LCLC-HAPF and those of the APF, LC-HAPF and LCL-HAPF are summarised in Table 2, in which the lower R_{dc_y}, A_{tten_y}, and R_{Ih_sy} indicate the higher dc-link voltage, weaker high-frequency attenuation capability and higher switching frequency sideband harmonic current in terms of the passive part of the LCLC-HAPF, respectively. From Table 2, it can be seen that:

(i) The LCLC-HAPF filter requires lower dc-link voltage compared with APF and LCL-HAPF.
(ii) The LCLC-HAPF has better high-frequency harmonic attenuations compared with APF and LC-HAPF.
(iii) The LCLC-HAPF obtains the minimum switching frequency sideband harmonic current compared with APF, LC-HAPF and LCL-HAPF, in which the ratio (R_{Ih_sy}) is less than 12.5, 25 and 50%, respectively.

Therefore, the LCLC-HAPF obtains low dc-link voltage, good high order harmonic attenuation and low switching frequency sideband harmonic current simultaneously, while the others cannot satisfy those characteristics simultaneously.

## 3 Damping strategy and stability analysis

In this section, the comparative analysis of the conventional damping methods and the proposed damping methods are separately provided in two sections. In Section 3.1, the conventional PD method is discussed. In Section 3.2, the proposed AD method for the LCLC-HAPF is analysed.
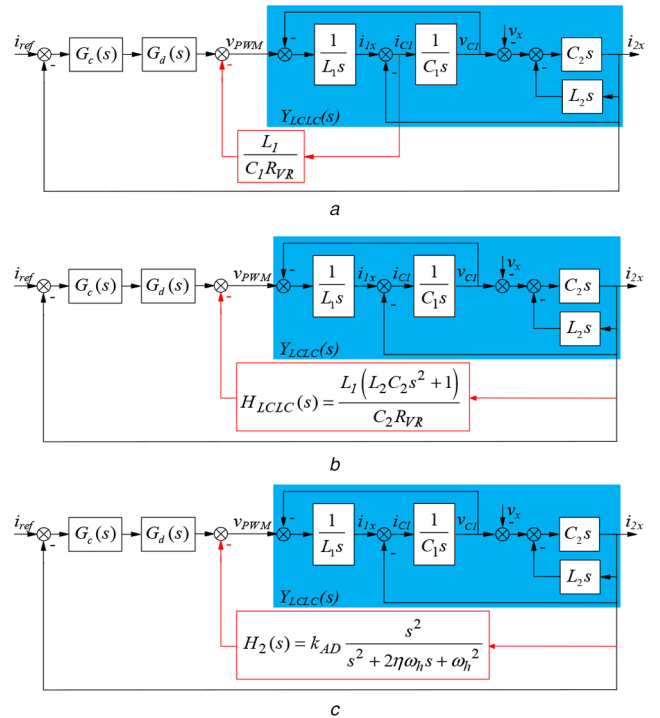
3.1 Conventional PD method

The conventional PD method that a resistor is inserted to series with C_1 [27], is shown in Fig. 5.

The transfer function $i_{2x}(s)/v_{invx\_LCLC}(s)$ of the LCLC filter with PD method in Fig. 5 can be deduced as follows:

$$\frac{i_{2x}(s)}{v_{invx\_LCLC}(s)} =$$
$$\frac{C_1 C_2 R_{PD} s^2 + C_2 s}{L_1 L_2 C_1 C_2 s^4 + L C_1 C_2 R_{PD} s^3 + (L_1 C_1 + L C_2)s^2 + C_1 R_{PD} s + 1} \quad (28)$$
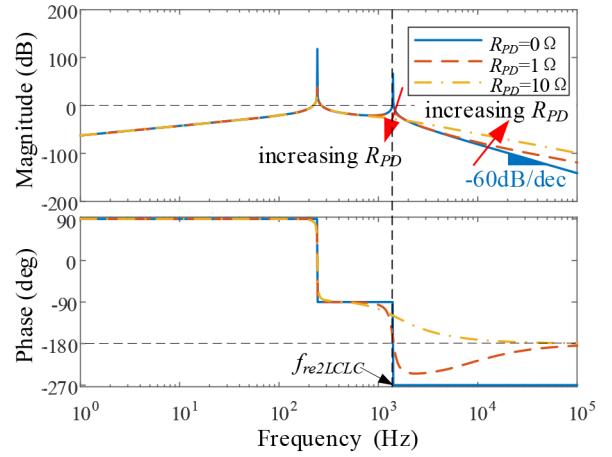
Fig. 6 *Bode diagram of the PD method when the R_{PD} are variables*

Fig. 7 *AD-based control block*
(a) Capacitor current feedback,
(b) Its equivalent grid-side current feedback,
(c) Proposed AD method with grid-side current feedback

The bode plots of $i_{2x}(s)/v_{invx\_LCLC}(s)$ with different R_{PD} values is illustrated in Fig. 6. It can be observed that the magnitude of this resonant peak can be damped below 0 dB at $f_{re2LCLC}$, which indicates the additional resistor R_{PD} can prevent the resonance phenomenon. However, the additional resistor's loss will be introduced substantially. In addition, Fig. 6 also shows that the slope of LCLC filter with PD method will be larger than −60 dB/dec as the damping resistance increases. In other words, the high-frequency attenuation capability is weakened by R_{PD}. Therefore, the PD method is not desirable.

3.2 Proposed AD method and system stability analysis

The structure of the AD method based on the capacitor current feedback is shown in Fig. 7a, where R_{VR} represents the value of VR in parallel with C_1. $G_c(s)$ is current controller. $G_d(s)$ is the control delay. By using the signal-flow graph method, the capacitor current feedback can also be transformed into grid-side current feedback as shown in Fig. 7b, in which the second-order derivative feedback $H_{LCLC}(s)$ can be expressed as:

$$H_{\text{LCLC}}(s) = \frac{L_1(L_2C_2s^2 + 1)}{C_2R_{\text{VR}}} \quad (29)$$

The bode plot of $H_{\text{LCLC}}(s)$ is shown in Fig. 8.

In the high-frequency region, the slope of the $H_{\text{LCLC}}(s)$ is -40 dB/dec. And the slope of $H_{\text{LCLC}}(s)$ is 0 dB/dec when the frequency is less than turning frequency f_{L2C2} in the following equation:

$$f_{L_2C_2} = \frac{1}{2\pi}\sqrt{1/L_2C_2} \quad (30)$$

However, $H_{\text{LCLC}}(s)$ seems to be difficult and unreliable no matter what digital control is adopted. Therefore, a simple digital implementation method is required to replace the one needs the $H_{\text{LCLC}}(s)$. The feasibility of using a first-order high-pass filter (FHPF) and a second-order high-pass filter (SHPF) to replace $H_{\text{LCLC}}(s)$ is discussed as the following.

The FHPF with phase-shifting feedback of the grid-side current for LCLC filter can be expressed as:

$$H_1(s) = -k_{\text{AD}}\frac{s}{s + \omega_h} \quad (31)$$

where k_{AD} represents the proportional feedback index, ω_h (in radians per second) or f_h (in hertz) is the turnover frequency of the FHPF. The negative sign is used for phase-shifting $180°$.

The SHPF transfer function can be expressed as:

$$H_2(s) = k_{\text{AD}}\frac{s^2}{s^2 + 2\eta\omega_h s + \omega_h^2} \quad (32)$$

where k_{AD} represents the proportional feedback factor, ω_h is the turnover frequency of the SHPF, and η is the damping coefficient of the SHPF. ω_h is recommend to 4 times $\omega_{re2\text{LCLC}}$, and η is equal to 0.707. In the high frequency region, the phase of the SHPF is consistent with $H_{\text{LCLC}}(s)$, therefore, no negative sign is required.

The comparison between $H_1(s)$ and $H_2(s)$ applied to the LCLC filter is shown in Fig. 8. It can be observed that $H_1(s)$ and $H_2(s)$ achieve the same damping effect at $f_{re2\text{LCLC}}$. However, the amplitude of $H_2(s)$ is 16 dB less than $H_1(s)$ at f_{L2C2}, which avoids the resonance activated at f_{L2C2} (This conclusion will be discussed next).

In Fig. 7, $Gc(s)$ is the proportional–integral (PI) controller, the transfer function of this PI controller is provided in

$$G_c(s) = K_p + \frac{K_i}{s} \quad (33)$$

where K_p is the proportional gain, K_i is the integral coefficient; $G_d(s)$ is the control delay in Fig. 7, which includes one sampling period T_s, and the modulator introduces another delay of $0.5T_s$. The total delay in the control loop is, thus, $1.5T_s$, expressed exponentially as:

$$G_d(s) = e^{-1.5T_s s} \quad (34)$$

The open-loop transfer function of Fig. 7b is:

$$G_{\text{open}}(s) = \frac{G_c(s)G_d(s)Y_{\text{LCLC}}(s)}{1 + G_d(s)Y_{\text{LCLC}}(s)H_{\text{LCLC}}(s)} \quad (35)$$

Replacing $H_{\text{LCLC}}(s)$ in (35) with $H_1(s)$ and $H_2(s)$, the open-loop stability of the two AD methods can be compared. Fig. 9a shows the bode plots that $H_{\text{LCLC}}(s) = H_1(s)$ when ω_h is $0.8\omega_{re2\text{LCLC}}$ and k_{AD} varies. After enabling AD, the open-loop transfer function adds two open-loop poles ($p = 2$ in Fig. 9). The gain of the resonant peak is decreased at $f_{re2\text{LCLC}}$, and the phase margin (PM) is always getting smaller when k_{AD} is increased. When k_{AD} is 30, the PM
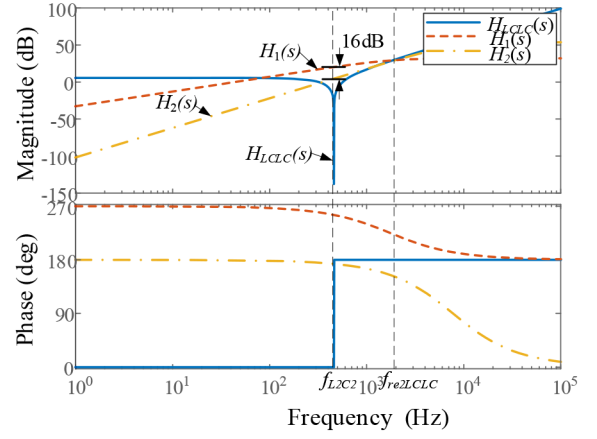

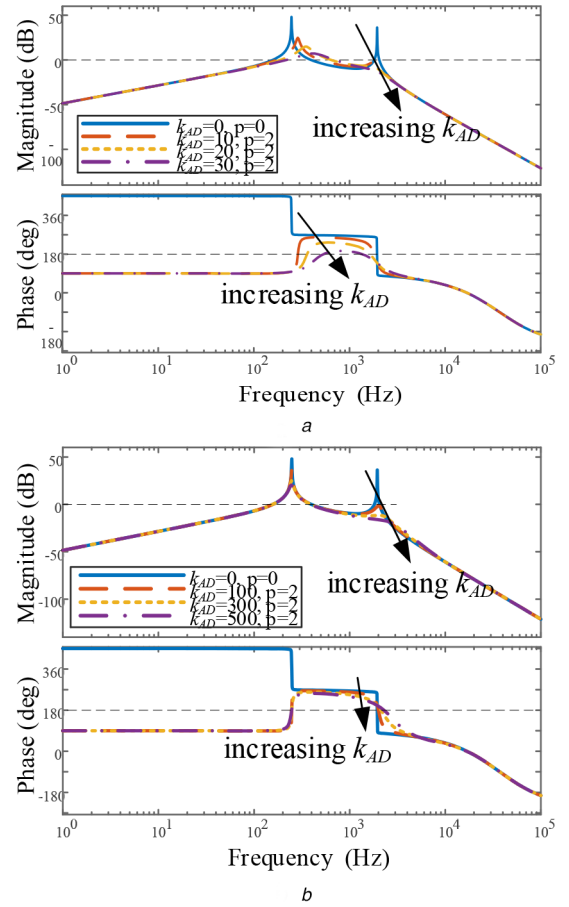**Fig. 8** *Comparison between $H_1(s)$ and $H_2(s)$ applied to LCLC filter*

**Fig. 9** *Bode plots of the open-loop transfer function with different AD methods*
(a) k_{AD} of $H_1(s)$ changes from small to large,
(b) k_{AD} of $H_2(s)$ changes from small to large

around f_{L2C2} is only $13.1°$, which does not meet the engineering requirements. Fig. 9b shows the bode plots that $H_{\text{LCLC}}(s) = H_2(s)$ when ω_h is $4\omega_{re2\text{LCLC}}$ and k_{AD} varies. With the increase of k_{AD}, the gain margin is increasing and the PM is little changing. Thus, the SHPF-based AD method is preferred as shown in Fig. 7c.

According to (35), the closed-loop transfer function can be written as:

$$G_{\text{closed}}(s)$$
$$= \frac{G_c(s)G_d(s)Y_{\text{LCLC}}(s)}{1 + G_c(s)G_d(s)Y_{\text{LCLC}}(s) + G_d(s)Y_{\text{LCLC}}(s)H_{\text{LCLC}}(s)} \quad (36)$$
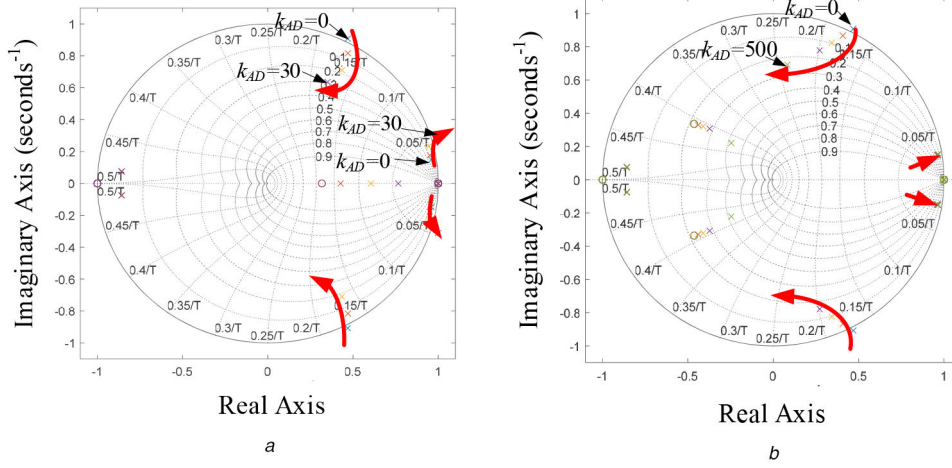
Fig. 10 *Pole-zero map by varying k_{AD} from small to large*
(a) FHPF-based AD,
(b) SHPF-based AD

Replacing $H_{LCLC}(s)$ in (36) with $H_1(s)$ and $H_2(s)$, the pole-zero map of the closed-loop system is shown in Fig. 10 using the Tustin discretisation method.

In Fig. 10*a*, two low-frequency poles appear on the outside of the unit circle as k_{AD} increases. Therefore, the system becomes unstable, and the unstable frequency is around f_{L2C2}. In Fig. 10*b*, the low-frequency pole respects insensitively as the k_{AD} increases.

In summary, the FHPF-based AD method will activate the low-frequency resonance at f_{L2C2}. The SHPF-based AD method can effectively solve this problem without activating low-frequency instability.

4 Parameter design of the LCLC filter

In the following, the design procedure of the LCLC filter parameters will be discussed in details.

4.1 Grid-side capacitance C_2

The C_2 should be designed to provide part of reactive power based on LCLC-HAPF capacity. The C_2 can be calculated as:

$$C_2 = \frac{120\% S_N}{6\pi f_1 V_s^2} \tag{37}$$

where S_N is apparent power rating of LCLC-HAPF, f_1 is the fundamental frequency. 120% is under compensation margin consideration. When the LCLC-HAPF's capacity is designed as 5 kVA, C_2 is selected as 120 μF.

4.2 DC-link voltage V_{dc}

A sufficient dc-link voltage is necessary to achieve good tracking performance. In Section 3, we have already analysed the required dc-link voltage. According to (14), (18) and (20), V_{dc} can be simplified as:

$$V_{dc} = \sqrt{6}\left(V_x - \frac{I_{2x}}{\omega_1 C_2}\right)(1 + M_r) \tag{38}$$

where M_r is the design margin for V_{dc}. The M_r includes not only the safety margin, but also the dc-link voltage requirement for the harmonic component. In this paper, a safe margin of 30% is chosen for reactive and harmonic compensation [22, 33]. Therefore, V_{dc} is selected as 220 V according to (38).

4.3 Inverter-side inductance L_1

The minimum inductance of L_1 can be selected as:

$$L_1 > \frac{V_{dc}}{2I_N k_{ripple} f_s} \tag{39}$$

where I_N is nominal current, k_{ripple} is the ratio of the maximum peak-to-peak current ripple to the rated fundamental current. The k_{ripple} is generally set to be less than 20%.

According to (39), L_1 should be larger than 1.96 mH. In this paper, $L_1 = 2.3$ mH is chosen.

4.4 Grid-side inductance L_2

The first resonance point $f_{re1LCLC}$ is determined by $L_1 + L_2$. The impedance of the LCLC filter is minimised at $f_{re1LCLC}$. Therefore, the required dc-link voltage to compensate harmonic current is minimum at $f_{re1LCLC}$

$$L_1 + L_2 = \frac{1}{(n*2\pi f_1)^2 C_2} \tag{40}$$

Considering the test load situation, $n = 5$ is selected and the value of $L_1 + L_2 = 3.38$ mH. When $L_1 = 2.3$ mH is designed before, thus $L_2 = 1.0$ mH is chosen.

4.5 Capacitance C_1

The limitation of capacitance C_1 can be estimated by $f_{re2LCLC}$. An applicable range of resonant frequency $f_{re2LCLC}$ reaches from twice of the highest compensated frequency f_{ch} to one-half of the switching frequency f_s, i.e. $2f_{ch} < f_{re2LCLC} < 0.5f_s$ [22]. According to (24), $C_1 = 10$ μF is selected, $f_{re2LCLC}$ is equal to 1950 Hz.

Based on the above analysis, LCLC filter parameters are listed in Table 3.

5 Simulation and experimental results

In this section, representative simulation and experimental results will be provided to verify the advantages and effectiveness of the LCLC-HAPF with the proposed AD method. The section mainly includes:

• The performance comparison among APF, LC-HAPF, LCL-HAPF with PD, LCLC-HAPF with PD and LCLC-HAPF with AD.
• Comparison of dc-link voltage requirement for LC-HAPF and LCLC-HAPF.
• Proposed AD methods for LCLC-HAPF.

The simulations are verified through PSCAD/EMTDC software. A 5 kVA three-phase three-wire LCLC-HAPF experimental prototype

**Table 3** Simulation and experimental parameters

Component	Description	Values
source voltage	V_x, f_1	230 V, 50 Hz
loads	L_R, R_R, L_{RL}, R_{RL}	160 mH, 1 Ω, 10 mH, 80 Ω
L filter	L, V_{dc}	3.3 mH, 720 V
LC filter	L, C_2, V_{dc}	3.3 mH, 120 μF, 220 V
LCL filter	L_1, C_1, L_2, V_{dc}	2.3 mH, 10 μF, 1.0 mH, 720 V
LCLC filter	L_1, L_2, C_1, C_2, V_{dc}	2.3 mH, 1 mH, 10 μF, 120 μF, 220 V
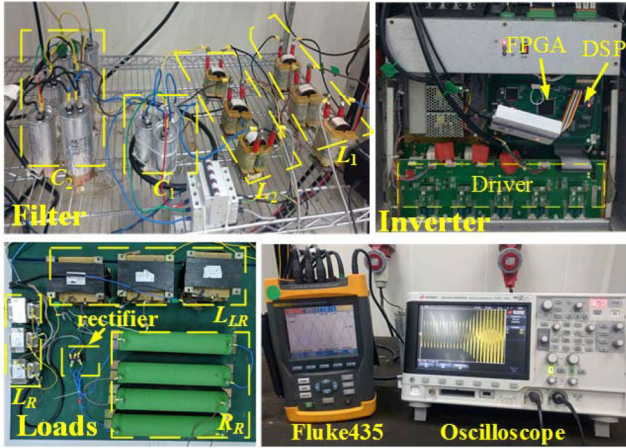
Fig. 11 *Experimental hardware platform setup of the 5 kVA prototype LCLC-HAPF*
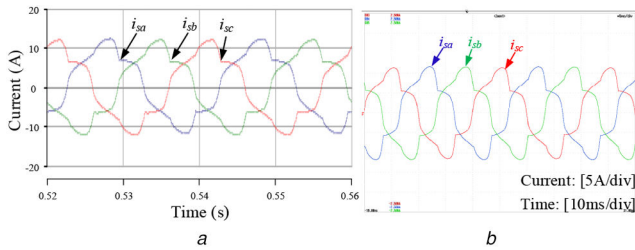
Fig. 12 *Source current before compensation*
(a) Simulation,
(b) Experiment
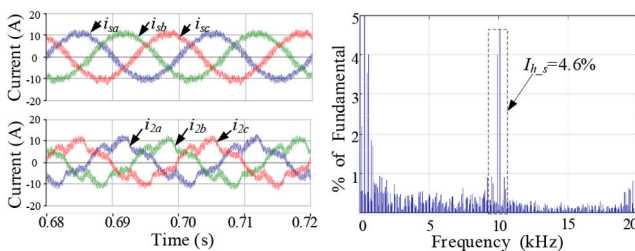
Fig. 13 *Simulated source current i_{sx} after compensation by APF, grid-side current i_{2x} and spectrum of i_{2a} of APF*

Fig. 14 *Simulated source current i_{sx} after compensation by HAPFs, grid-side current i_{2x} and spectrum of i_{2a} of HAPFs*

(a) LC-HAPF,
(b) LCL-HAPF with PD,
(c) LCLC-HAPF with PD,
(d) LCLC-HAPF with AD

is designed and constructed in the laboratory as shown in Fig. 11. The digital control system consists of one digital signal processor (DSP) TMS320F28335, and one field-programmable gate array (FPGA) EP1C6Q240I7. The DSP mainly does control algorithms, and the FPGA is mainly used to complete logic functions, such as protection. The sampling and switching frequency are 10 kHz. The simulation and experimental parameters are given in Table 3. The APF, LC-HAPF and LCL-HAPF topologies can be obtained by bypassing C_1 and/or C_2. The LCLC-HAPF topology becomes APF topology when C_1 and C_2 are bypassed. The LCLC-HAPF topology becomes LC-HAPF topology when C_1 is bypassed. The LCLC-HAPF topology becomes LCL-HAPF topology when C_2 is bypassed.

The three-phase source current waveforms before compensation are shown in Fig. 12. The source currents are distorted due to the presence of non-linear loads.

5.1 Performance comparison

The performance comparisons through simulation and experiment will be demonstrated in this section.

Figs. 13 and 14 illustrate the comparison of steady-state compensation performance. As shown in Figs. 13 and 14, the harmonic compensation performance of different compensators is almost the same. However, the APF has the highest switching
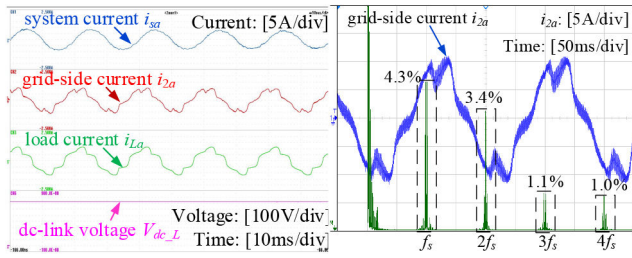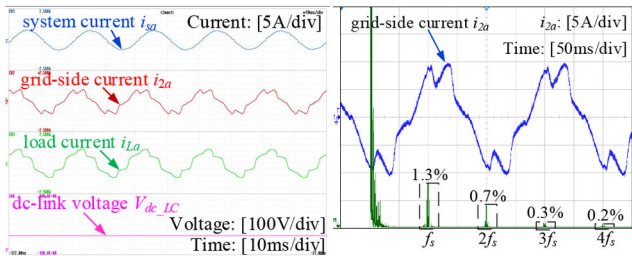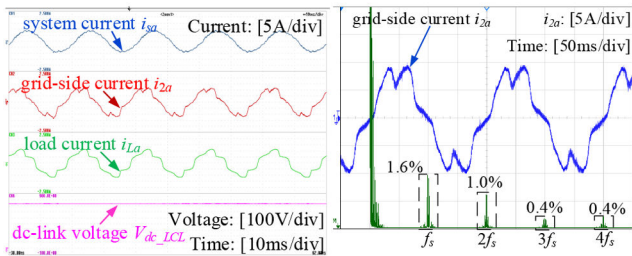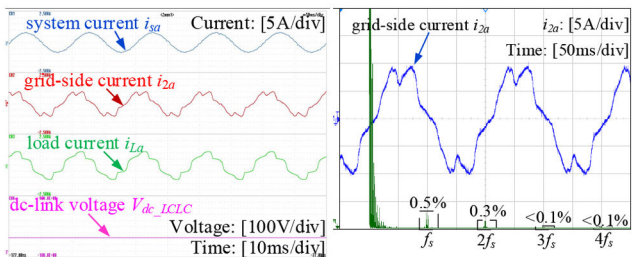
1214

Fig. 15 *Experimental source current i_{sx} after compensation by APF, grid-side current i_{2x} and spectrum of i_{2a} of APF*
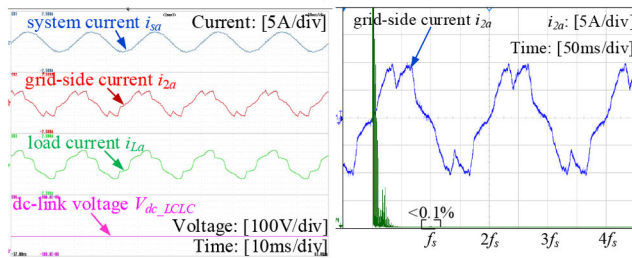

a

b

c

d

Fig. 16 *Experimental source current i_{sx} after compensation by HAPFs, grid-side current i_{2x} and spectrum of i_{2a} of HAPFs*
(a) LC-HAPF,
(b) LCL-HAPF,
(c) LCLC-HAPF with PD,
(d) LCLC-HAPF with AD

frequency sideband harmonic component I_{h_s}(4.6%) in Fig. 13, followed by LC-HAPF (1.4%) in Fig. 14*a*, LCL-HAPF with PD (1.3%) in Fig. 14*b*, LCLC-HAPF with PD (0.6%) in Fig. 14*c* and LCLC-HAPF with AD (0.1%) in Fig. 14*d*.

In Figs. 15 and 16, the experimental source current after compensation i_{sx}, grid-side current i_{2x} and spectrum of i_{2a} of different compensators are presented.
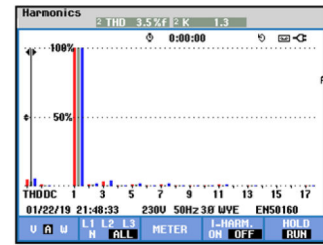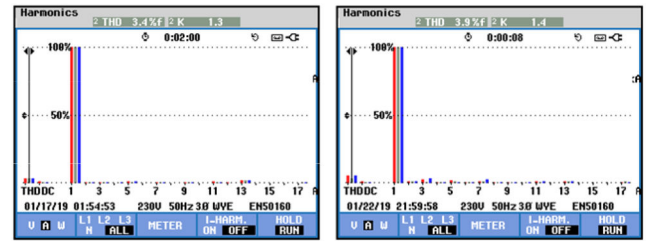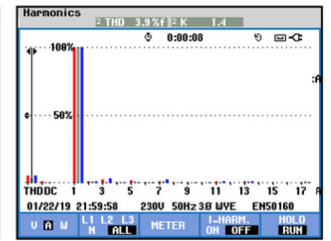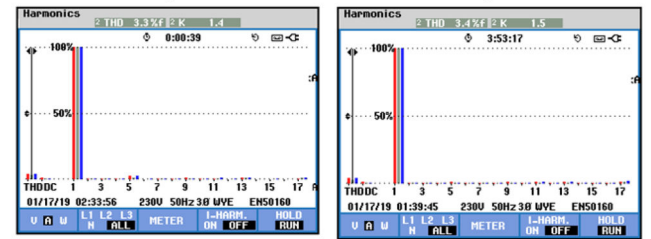

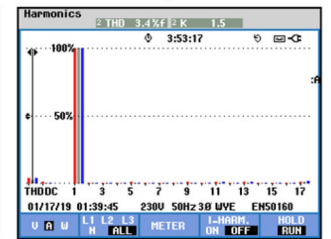**Fig. 17** *THD of experimental i_{sx} after compensation by APF*

a

b

c

d

Fig. 18 *THD of experimental i_{sx} after compensation by*
(a) LC-HAPF,
(b) LCL-HAPF,
(c) LCLC-HAPF with PD,
(d) LCLC-HAPF with AD

The experimental results illustrate the same conclusions as the simulation results, that is, the harmonic compensation performance of different compensators is almost the same. The total harmonics distortion (THD) of i_{sx} compensated by different compensators are shown in Figs. 17 and 18. However, the APF obtains highest switching frequency sideband harmonic component I_{h_s} (4.3%) in Fig. 15 and the LCLC-HAPF with AD obtains smallest switching frequency sideband harmonic component (<0.1%) in Fig. 16*d*.

Table 4 summarises the simulation and experimental results. The power loss P_{Loss} is measured by YOKOGAWA WT1800 PRECISION ANALYZER. The I_{h_s} in Table 4 is switching frequency sideband harmonic measured by Oscilloscope (KEYSIGHT DSOX2012A). The THD_{is} results are measured by Fluke 435.

The loss of the APF and LCL-HAPF are much higher than those of the LC-HAPF and LCLC-HAPF. The main reason is that the dc-link voltage of APF and LCL-HAPF is 720 V, while the dc-link voltage of LC-HAPF and LCLC-HAPF is only 220 V. Compared with LCLC-HAPF with PD, the loss of LCLC-HAPF with AD is slightly reduced from 77.7 to 73.3 W. It shows that LCLC-HAPF with AD obtains better efficiency.

5.2 Comparison of required dc-link voltage

The comparison of the minimum dc-link voltage requirement for LC-HAPF and LCLC-HAPF will be discussed in this section.

Figs. 19 and 20 show that the simulated and experimental compensation performance of LC-HAPF and LCLC-HAPF meet the IEEE Standard (THD < 5%), when the dc-link voltage is 200 V. In order to verify if they can operate at a lower dc-link voltage, the dc-link voltage is decreased to 195 V. However, the compensation performance of LC-HAPF become worse (THD is increased from 4.8 to 6.7%). However, when the same situation is applied to LCLC-HAPF, the performance of THD is only increased by 0.1%.

Table 4 Simulation and experimental results of different compensators

| Compensator	Simulation			Experiment				
	Q_{out}, kVar	I_{h_s}, %	V_{dc}, V	Q_{out}, kVar	THD$_{is}$, %	I_{h_s}, %	P_{Loss}, W	V_{dc}, V
APF	4.01	4.6	720	4.5384	3.5	4.3	218.1	720
LC-HAPF	4.16	1.4	220	4.4295	3.4	1.6	74.7	220
LCL-HAPF	4.06	1.3	720	4.3886	3.9	1.3	253.7	720
LCLC-HAPF (PD)	4.13	0.6	220	4.5692	3.3	0.5	77.2	220
LCLC-HAPF (AD)	4.14	0.1	220	4.5804	3.4	<0.1	73.3	220
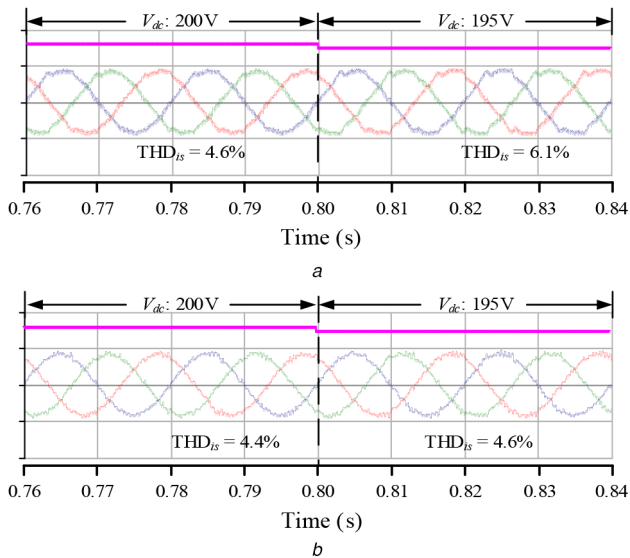
Fig. 19 *Simulation results after compensation with different dc-link voltages*
(a) LC-HAPF,
(b) LCLC-HAPF
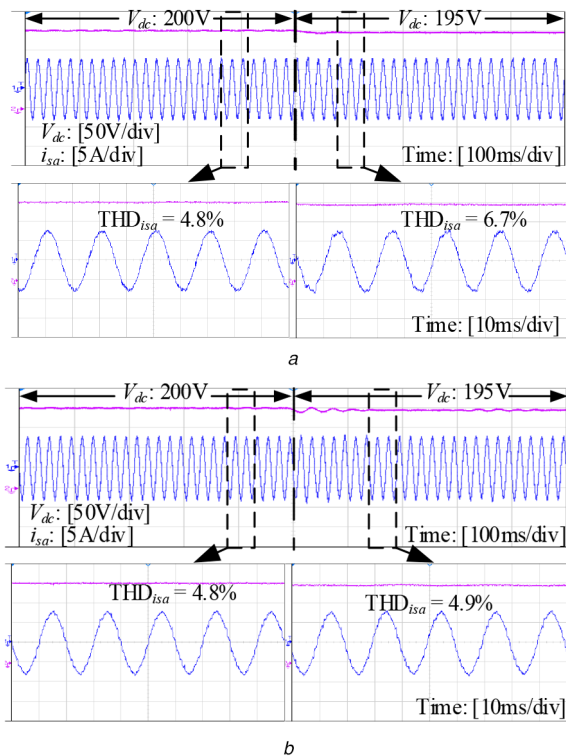
Fig. 20 *Experimental results after compensation with different dc-link voltages*
(a) LC-HAPF,
(b) LCLC-HAPF

So that, it shows that, LCLC-HAPF required less dc-link voltage than LC-HAPF.
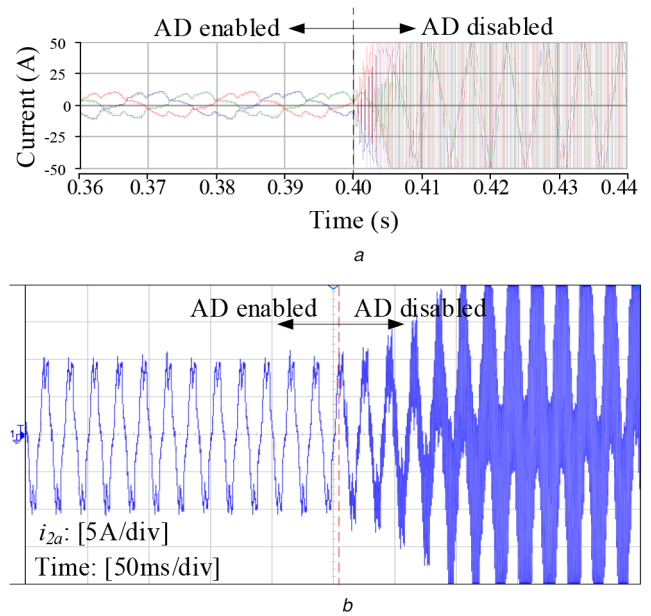
Fig. 21 *Waveform of i_{2a} for LCLC-HAPF from AD enabled to AD disabled*
(a) Simulation waveforms,
(b) Experiment waveforms

5.3 Effectiveness of proposed AD method

The results indicate that LCLC-HAPF with AD has better performance than LCLC-HAPF with PD in Section 5.1. Further, Fig. 21 shows the dynamic process of both simulation and experiment from AD enabled to AD disabled, where the resonance occurs after AD disabled. Consequently, the proposed SHPF-based AD method for LCLC-HAPF can effectively solve the stability problem.

6 Conclusion

A new LCLC-HAPF with new AD methods and corresponding parameter design have been proposed in this paper. Through comparisons among APF, LC-HAPF, LCL-HAPF and LCLC-HAPF, the proposed LCLC-HAPF brings some advantages, such as low dc-link voltage, outstanding attenuation characteristics on high order harmonic and small switching frequency sideband harmonic current. By applying the proposed AD method to LCLC-HAPF, the resonance phenomenon of the LCLC-HAPF has been prevented, which avoids not only extra resistors but also high-precision sensors. In addition, a suitable parameter selecting criteria and a design procedure of the LCLC filter are also introduced. Finally, the advantages and effectiveness of the LCLC-HAPF with AD are verified by both comparative simulation and experiment with APF, LC-HAPF and LCL-HAPF with PD and LCLC-HAPF with PD.

7 Acknowledgments

8 References

[1] Senini, S. T., Wolfs, P. J.: 'Systematic identification and review of hybrid active filter topologies'. Proc. IEEE 33rd Annual Power Electronics Specialists Conf. (PESC), Cairns, Australia, Jun 2002, pp. 394–399

[2] Wang, L., Lam, C. S., Wong, M. C.: 'Design of a thyristor controlled LC filter for wind farm dynamic reactive power compensation in smart grid', *IEEE Trans. Smart Grid*, 2017, **8**, (1), pp. 409–417

[3] Dionise, T. J.: 'Assessing the performance of a static VAR compensator for an electric arc furnace', *IEEE Trans. Ind. Appl.*, 2014, **50**, (3), pp. 1619–1629

[4] Terriche, Y., Mutarraf, M., Mehrzadi, M.*, et al.*: 'Adaptive CDSC-based open-loop synchronization technique for dynamic response enhancement of active power filters', *IEEE. Access.*, 2019, **7**, pp. 96743–96752

[5] Luo, A., Tang, C., Shuai, Z. K.*, et al.*: 'A novel three-phase hybrid active power filter with a series resonance circuit tuned at the fundamental frequency', *IEEE Trans. Ind. Electron.*, 2009, **56**, (7), pp. 2431–2440

[6] Ferreira, S.C., Gonzatti, R. B., Pereira, R. R.*, et al.*: 'Finite control set model predictive control for dynamic reactive power compensation with hybrid active power filters', *IEEE Trans. Ind. Electron.*, 2018, **65**, (3), pp. 2608–2617

[7] Luo, A., Shuai, Z., Zhu, W.*, et al.*: 'Combined system for harmonic suppression and reactive power compensation', *IEEE Trans. Ind. Electron.*, 2009, **56**, (2), pp. 418–428

[8] Chau, M., Luo, A., Ma, F.*, et al.*: 'Online control method with time-delay compensation for hybrid active power filter with injection circuit', *IET Power Electron.*, 2012, **5**, (8), pp. 1472–1482

[9] Luo, A., Peng, S., Wu, C.*, et al.*: 'Power electronic hybrid system for load balancing compensation and frequency-selective harmonic suppression', *IEEE Trans. Ind. Electron.*, 2012, **59**, (2), pp. 723–732

[10] Lam, C. S., Wong, M. C., Han, Y. D.: 'Hysteresis current control of hybrid active power filters', *IET Power Electron.*, 2012, **5**, (7), pp. 1175–1187

[11] Lam, C.-S., Choi, W.-H., Wong, M.-C.*, et al.*: 'Adaptive DC-link voltage-controlled hybrid active power filters for reactive power compensation', *IEEE Trans. Power Electron.*, 2012, **27**, (4), pp. 1758–1772

[12] Dai, N.-Y., Zhang, W.-C., Wong, M.-C.*, et al.*: 'Analysis, control and experimental verification of a single-phase capacitive-coupling grid-connected inverter', *IET Power Electron.*, 2015, **8**, (5), pp. 770–782

[13] Tareen, W. U. K., Mekhielf, S.: 'Three-phase transformerless shunt active power filter with reduced switch count for harmonic compensation in grid-connected applications', *IEEE Trans. Power Electron.*, 2018, **33**, (6), pp. 4868–4881

[14] Lam, C. S., Cui, X. X., Choi, W. H.*, et al.*: 'Minimum inverter capacity design for LC-hybrid active power filters in three-phase four-wire distribution systems', *IET Power Electron.*, 2012, **5**, (7), pp. 956–968

[15] Wang, L., Lam, C. S., Wong, M. C.: 'Multifunctional hybrid structure of SVC and capacitive grid-connected inverter (SVC//CGCI) for active power injection and nonactive power compensation', *IEEE Trans. Ind. Electron.*, 2019, **66**, (3), pp. 1660–1670

[16] Rahmani, S., Hamadi, A., Al-Haddad, K.*, et al.*: 'A combination of shunt hybrid power filter and thyristor-controlled reactor for power quality', *IEEE Trans. Ind. Electron.*, 2014, **61**, (5), pp. 2152–2164

[17] Wang, L., Lam, C. S., Wong, M. C.: 'Analysis, control and design of hybrid grid-connected inverter for renewable energy generation with power quality conditioning', *IEEE Trans. Power Electron.*, 2018, **33**, (8), pp. 6755–6768

[18] Wang, L., Lam, C. S., Wong, M. C.: 'Minimizing inverter capacity design and comparative performance evaluation of SVC-coupling hybrid active power filters', *IEEE Trans. Power Electron.*, 2019, **34**, (2), pp. 1227–1242

[19] IEEE Standard 519-2014: 'IEEE recommended practices and requirements for harmonic control in electrical power systems', 2014

[20] Fang, J., Li, X., Yang, X.*, et al.*: 'An integrated trap-LCL filter with reduced current harmonics for grid-connected converters under weak grid conditions', *IEEE Trans. Power Electron.*, 2017, **32**, (11), pp. 8446–8457

[21] Park, K. B., Kieferndorf, F. D., Drofenik, U.*, et al.*: 'Weight minimization of LCL filters for high power converters: impact of PWM method on power loss and power density', *IEEE Trans. Ind. Appl.*, 2017, **53**, (3), pp. 2282–2296

[22] Liu, Q., Peng, L., Kang, Y.*, et al.*: 'A novel design and optimization method of an LCL filter for a shunt active power filter', *IEEE Trans. Ind. Electron.*, 2014, **61**, (8), pp. 4000–4010

[23] Kim, Y., Kim, H.: 'Optimal design of LCL filter in grid-connected inverters', *IET Power Electron.*, 2019, **12**, (7), pp. 1774–1782

[24] Yang, L., Yang, J.: 'A robust dual-loop current control method with a delay-compensation control link for LCL-type shunt active power filters', *IEEE Trans. Power Electron.*, 2019, **34**, (7), pp. 6183–6199

[25] Yeetum, W., Kinnares, V.: 'Parallel active power filter based on source current detection for antiparallel resonance with robustness to parameter variations in power systems', *IEEE Trans. Ind. Electron.*, 2019, **66**, (2), pp. 876–886

[26] Liu, T., Liu, J., Liu, Z.*, et al.*: 'A study of virtual resistor-based active damping alternatives for LCL resonance in grid-connected voltage source inverters', *IEEE Trans. Power Electron.*, 2020, **35**, (1), pp. 247–262

[27] Kumar, C., Mishra, M.: 'An improved hybrid DSATCOM topology to compensate reactive and nonlinear loads', *IEEE Trans. Ind. Electron.*, 2014, **61**, (12), pp. 6517–6527

[28] Chen, H., Cheng, P., Wang, X.*, et al.*: 'A passivity-based stability analysis of the active damping technique in the offshore wind farm applications', *IEEE Trans. Ind. Appl.*, 2018, **54**, (5), pp. 5074–5082

[29] Li, X., Wu, X., Geng, Y.*, et al.*: 'Wide damping region for LCL-type grid-connected inverter with an improved capacitor-current-feedback method', *IEEE Trans. Power Electron.*, 2015, **30**, (9), pp. 5247–5259

[30] Mohamed, Y. A.-R. I.: 'Suppression of low- and high-frequency instabilities and grid-induced disturbances in distributed generation inverters', *IEEE Trans. Power Electron.*, 2011, **26**, (12), pp. 3790–3803

[31] Dannehl, J., Fuchs, F., Hansen, S.*, et al.*: 'Investigation of active damping approaches for PI-based current control of grid-connected PWM converters with LCL filters'. Proc. IEEE ECCE, San Jose, CA, USA, Sep 2009, pp. 2998–3005

[32] Xin, Z., Loh, P. C., Wang, X.*, et al.*: 'Highly accurate derivatives for LCL-filtered grid converter with capacitor voltage active damping', *IEEE Trans. Power Electron.*, 2016, **31**, (5), pp. 3612–3625

[33] Xu, J., Xie, S., Tang, T.: 'Active damping-based control for grid-connected LCL-filtered inverter with injected grid current feedback only', *IEEE Trans. Ind. Electron.*, 2014, **61**, (9), pp. 4746–4758

[34] Alexander, C. K., Sadiku, M. N. O.: '*Fundamentals of electric circuits*' (McGraw-Hill Education, USA, 2016, 6th edn.)

[35] Holmes, D. G., Lipo, T. A.: '*Pulse width modulation for power converters-principle and practice*' (IEEE Press, USA, 2003)